Fast and Chaotic Fiber-Based Nonlinear Polarization Scrambler

Massimiliano Guasoni, Pierre-Yves Bony, Marin Gilles, Antonio Picozzi, Julien Fatome

Fast and Chaotic Fiber-Based Nonlinear Polarization Scrambler

M. Guasoni, P-Y. Bony, M. Gilles, A. Picozzi, and J. Fatome*

Laboratoire Interdisciplinaire Carnot de Bourgogne,
UMR 6303 CNRS, Université Bourgogne Franche-Comté,
9 av. Alain Savary Dijon 21078, France

*jfatome@u-bourgogne.fr

We report a simple and efficient all-optical polarization scrambler based on the nonlinear interaction in an optical fiber between a signal beam and its backward replica which is generated and amplified by a reflective loop. When the amplification factor exceeds a certain threshold, the system exhibits a chaotic regime in which the evolution of the output polarization state of the signal becomes temporally chaotic and scrambled all over the surface of the Poincaré sphere. We numerically derive some design rules for the scrambling performances of our device which are well confirmed by the experimental results. The polarization scrambler has been successfully tested on a 10-Gbit/s On/Off Keying Telecom signal, reaching scrambling speeds up to 500-krad/s, as well as in a wavelength division multiplexing configuration. A different configuration based on a following cascade of polarization scramblers is also discussed numerically, which leads to an increase of the scrambling performances.

I. Introduction

The ability to randomly scramble the state-of-polarization (SOP) of a light beam is an important issue that encounters numerous applications in photonics. Polarization scrambling is indeed mainly implemented to ensure polarization diversity in optical telecommunication systems so as to combat deleterious polarization effects and provide mitigation of polarization mode dispersion (PMD) and polarization dependent loss or gain [1]. For instance, polarization scrambling has been exploited to avoid polarization hole burning in Erbium doped fiber amplifiers (EDFA) [2], and has allowed washing out PMD-induced error bursts within forward error correction frames [3]. Furthermore, polarization scrambling is a mandatory procedure when testing the performances of polarization-sensitive fiber systems or optical components. For that purpose, the SOP changing rate (i.e. the scrambling speed) induced by the scrambler device should be as high as some hundreds of Krad/s in order to match the scale of fast polarization changes encountered in high-speed fiber optic systems [4].

Traditionally, polarization scrambler technologies are based on the cascade of fiber resonant coils, of rotating half and quarter alternated wave-plates, or of fiber squeezers as well as opto-electronic elements [5-14]. In most of these devices an external voltage is applied: it drives the rotation of the wave-plates, the squeezing of the fiber as well as the expansion of the piezo-electric coils, so that the scrambling performances are directly controlled by means of this driving voltage. These opto-electronic technologies have been successfully implemented into commercially available devices capable to provide records of scrambling speeds, reaching several of Mrad/s [10-13] with moderate costs and lower power consumptions.

On the other hand, new techniques have emerged in the last few years exploring the possibility to all-optically randomize the polarization state of an incident signal [14-17]. The present work has been carried out in this context of fundamental research and aims to explore an alternative and complementary approach to current opto-electronic solutions. More precisely, here we report a numerical and experimental description of an all-optical polarization scrambler based on the nonlinear Kerr effect occurring in optical fibers. This device exhibits a chaotic dynamics, which could open the way towards a chaos-based scrambling technology in optical fibers not yet explored. Furthermore, the present device could be qualified as "home-made" since it is essentially based on standard components usually available in any Labs working in the field of nonlinear optics and optical communications.

The basic principle of this device was first established in refs. [16] and [17], where it has been exploited in order to demonstrate a transparent method of temporal spying and concealing process for optical communications. Basically, it consists in an additional operating mode, namely the chaotic mode, of the device called Omnipolarizer, originally conceived to operate as an all-optical polarization attractor and beam splitter [18, 19].

In this paper we gain a deeper insight into the physics of this all-optical polarization scrambler. We go significantly beyond our previous works reported in refs. [16, 17], especially by deriving numerically some design rules for the scrambling performances as well as testing our system in a wavelength division multiplexing (WDM) transmission and proposing a new configuration, based on a cascade of scramblers, which could greatly improve the scrambling performances.

The paper is organized as follows. First of all in section II, we introduce the principle of operation of our polarization

scrambler. Then in section III we describe the experimental setup. In section IV we model and discuss the dynamics of our device and derive expressions for two important threshold parameters, which allow us to carefully discuss the transition of the system from a polarization attraction regime to the chaotic scrambling regime. In section V we report our experimental results in the CW regime and for a 10-Gbit/s On/Off keying (OOK) Telecom signal. Then, in section VI, we find an estimation of the scrambling performances as a function of the system parameters, and in section VII we numerically discuss the efficiency improvement provided by a cascade of scramblers. In section VIII we provide experimental evidences of the compatibility of our all-optical scrambler for WDM applications and finally in the last section, we summarize our work and outline some possible ways of improvement.

II. Principle of Operation

The principle of operation of the all-optical scrambler is schematically displayed in Fig. 1. It basically consists in a nonlinear Kerr medium, here an optical fiber, in which an initial forward signal **S** with a fixed polarization-state interacts nonlinearly due to a cross-polarization interaction with its own backward replica **J** generated at the fiber end by means of an amplified reflective loop. A strong power imbalance between the two beams is applied, which can actually lead to a chaotic polarization dynamics for both the forward and backward output fields [20, 21].

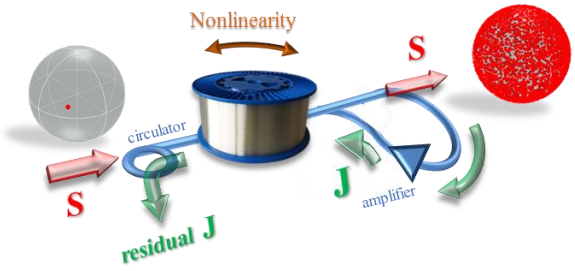

Fig. 1. Principle of operation.

In some of our previous works [18, 19, 22, 23] we have already identified some particular regimes associated to this kind of counter-propagative cross-polarization interaction. For example, we have put in evidence that typically for nearly equal forward and backward beam powers, the stable stationary singular states of the system play the role of natural polarization attractors for the output signals. Generally these stationary states $\mathbf{S}_{stat}$ and $\mathbf{J}_{stat}$ can be computed as a function of the system parameters, such as the forward and backward powers as well as the fiber length L.

In order to illustrate that point, panels (a-c) of Fig. 2 display the attraction process undergone by an input signal towards a stable stationary state for nearly equal counter-propagative beam powers. For clearness, only a single Stokes component of **S** and **J** is represented, let us say S_1 and J_1 (solid line), as well as for $\mathbf{S}_{stat}$ and $\mathbf{J}_{stat}$, let us say $S_{1,stat}$ and $J_{1,stat}$ (in circles). We can then observe the spatial evolutions of S_1 and J_1 along the fiber length for 3 consecutive times $t_A < t_B < t_C$. In the time slot

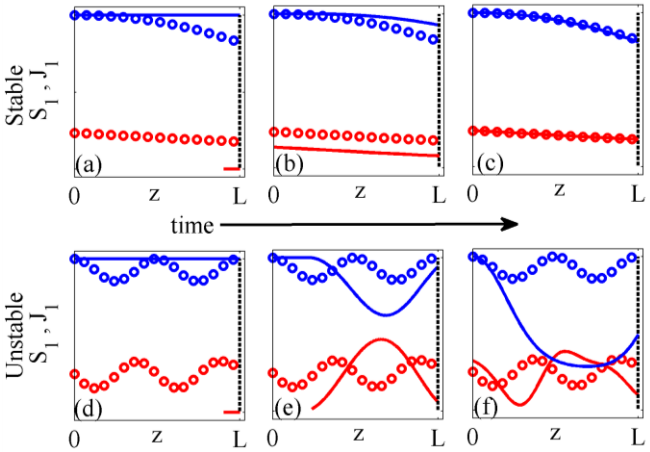

Fig. 2. Spatial evolution along the fiber length of the Stokes components S_1 (blue solid lines) and J_1 (red solid lines) at 3 consecutive instants t_A (a-d), t_B (b-e) and t_C (c-f). Corresponding stationary solutions $S_{1,stat}$ and $J_{1,stat}$ are represented in circles. In the case of panels (a-c) the counter-propagating waves have almost the same power so that the stationary solutions are stable. Consequently S_1 and J_1 gradually converge in time towards $S_{1,stat}$ and $J_{1,stat}$ respectively. Conversely, in the case depicted by panels (d-f) the stationary solutions are unstable and therefore no attraction process occurs.

$0 < t < L/c$, where c is the speed of light in the fiber, the signal **S** propagates unaffected by nonlinear effects, since **J** has not yet been generated at the opposite end of the fiber. For illustration purpose, panel (a) shows the corresponding spatial profile of S_1 at instant t_A slightly larger than L/c: the backward replica J_1 has just been reflected and starts to counter-propagate. Afterward, (panel (b)), the cross-polarization interaction between **S** and **J** makes them to gradually converge towards the stable stationary states of the system. Finally, at the instant t_C (panel (c)) the spatial profiles of **S** and **J** almost perfectly match the stationary solutions and do not evolve substantially in the subsequent instants. Therefore, in this instance the stable stationary states act as asymptotic attractors [19].

On the contrary, for large power unbalances between counter-propagating fields, the stationary states become unstable. As depicted by panels (d-f) the forward and backward beams are then no longer attracted towards a stationary state solution: both beams oscillate in time without reaching a fixed state. We will see in the following that the forward polarization at the exit of the fiber varies endlessly in time and becomes temporally scrambled as a result of a chaotic dynamics all over the surface of the Poincaré sphere. This constitutes the basic principle of our all-optical polarization scrambler.

III. Experimental Implementation

The experimental implementation of the proposed scrambler is schematically displayed in Fig. 3.

For fundamental studies, the initial signal consists in a fully polarized 100-GHz-bandwidth partially incoherent wave, centered at 1550 nm. This incident signal is generated from an Erbium-based amplified spontaneous noise source (ASE) filtered in the spectral domain by means of a wavelength-demultiplexer followed by an inline polarizer. This large bandwidth input signal is used to avoid any impairment due to the stimulated Brillouin backscattering occurring in the fiber under-test.

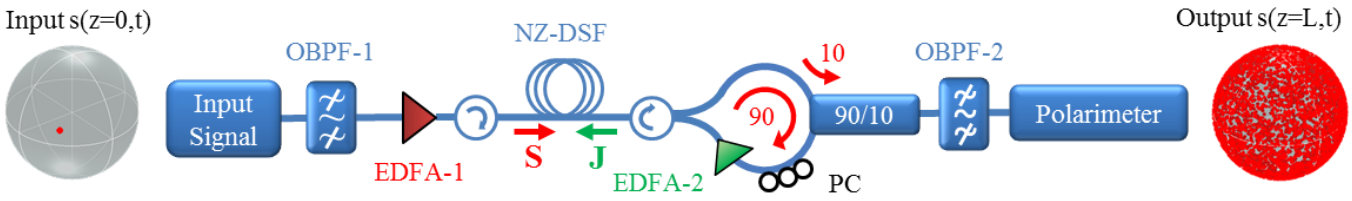

Fig. 3 Experimental setup of the chaotic polarization scrambler under study. PC: Polarization Controller, OBPF: Optical bandpass filter. The two Poincaré spheres illustrate the distribution of the Stokes vector of the forward beam at the input (fully polarized) and at the output (scrambled over the sphere), respectively.

In a second step, in order to evaluate the performance of this all-optical scrambler for Telecom applications, the incoherent wave is replaced by a 10-Gbit/s OOK signal at 1550 nm. This return-to-zero (RZ) optical signal is generated from a 10-GHz mode-locked fiber laser delivering 2.5-ps pulses at 1550 nm. The spectrum of this initial pulse train is shaped thanks to a liquid-crystal based optical filter to temporally broad the pulses to 20 ps. The resulting 10-GHz pulse train is intensity modulated thanks to a $LiNbO_3$ Mach-Zehnder modulator driven by a high-speed RF pattern generator. The input signal is then amplified by means of an Erbium doped fiber amplifier (EDFA-1) before injection into the fiber under-test thanks to an optical circulator. Note that this optical circulator is mainly used so as to suppress the residual counter-propagating signal replica.

In order to characterize the dynamics of our polarization scrambler, two fibers were tested. Fiber-1 corresponds to a 5.3-km long non-zero dispersion shifted fiber (NZ-DSF) characterized by a chromatic dispersion of -1 ps/nm/km at 1550 nm, linear losses 0.24 dB/km and a nonlinear coefficient $\gamma = 1.7$ $W^{-1}km^{-1}$. Fibre-2 is a reduced slope telecom fiber (OFS-TW-SRS) characterized by L = 10 km, a chromatic dispersion of -2.8 ps/nm/km, $\gamma = 1.7$ $W^{-1}km^{-1}$ and losses of 0.2 dB/km.

The reflective-loop setup which enables to produce the backward replica at the fiber end consists in an optical circulator followed by a polarization controller (PC) as well as a second Erbium amplifier (EDFA-2). Note that the EDFA-2 provides the gain of the backward wave, which allows us to finely adjust the power imbalance with respect to the forward signal. A 90/10 coupler is also inserted into the loop to send the resulting scrambled signal for analysis. The forward output signal is optically filtered at λ_{OBPF-2} = 1550 nm (OBPF-2, bandwidth 100-GHz) to remove the excess of amplified spontaneous noise emission outside the signal bandwidth. The state-of-polarization of the output signal is finally characterized by means of a standard commercial polarimeter.

IV. System Dynamics

In the following, we indicate with $\mathbf{S} = [S_1, S_2, S_3]$ and $\mathbf{J} = [J_1, J_2, J_3]$ the Stokes vectors for the forward and backward beams, respectively. Consequently, the normalized unitary vectors $\mathbf{s} = \mathbf{S}/|\mathbf{S}|$ and $\mathbf{j} = \mathbf{J}/|\mathbf{J}|$ indicate the corresponding SOP.

The dynamics of the system is mainly driven by the amplification factor g of the loop defined by the power ratio between the backward and forward signals at the fiber output: $g = |\mathbf{J}(z=L,t)| \,/\, |\mathbf{S}(z=L,t)|$, where z indicates the propagation length along the fiber. In practice, the coefficient g can be directly adjusted by means of the EDFA-2. Furthermore, in ref. [17], we have pointed out the existence of two threshold values for the parameter g, defined as g_A and g_C, that allow us to distinguish three different operating regimes, namely the *attraction* regime ($g < g_A$), the *transient* regime ($g_A < g < g_C$) and the *chaotic* regime ($g > g_C$).

The evolutions of **S** and **J** along the fiber length are governed by the following coupled equations [24]:

$$\begin{aligned} c^{-1}\partial_t \mathbf{S} + \partial_z \mathbf{S} &= \mathbf{S} \times \mathrm{D}\mathbf{J} - \alpha \mathbf{S} \\ c^{-1}\partial_t \mathbf{J} - \partial_z \mathbf{J} &= \mathbf{J} \times \mathrm{D}\mathbf{S} - \alpha \mathbf{J} \end{aligned} \qquad (1)$$

where $\mathrm{D} = \gamma\,\mathrm{diag}(-8/9, 8/9, -8/9)$ is a diagonal matrix, γ and α are the nonlinear Kerr coefficient and the propagation losses of the fiber, respectively, and c is the speed of light in the fiber. According to Eqs.(1) the average powers $P_S(z) = \langle|\mathbf{S}(z,t)|\rangle$ and $P_J(z) = \langle|\mathbf{J}(z,t)|\rangle$ (the brackets $\langle\rangle$ denote a temporal averaging) are individually conserved except for the propagation losses, indeed $P_S(z) = P_S(0)\exp(-\alpha z)$ and $P_J(z) = P_J(L)\exp(\alpha(z-L))$.

In our numerical simulations we solve Eqs.(1) subject to the boundary condition $\mathbf{J}(z=L,t) = gR\mathbf{S}(z=L,t)$, in which R is a 3x3 matrix modeling the polarization rotation in the reflective-loop, which is imposed by the circulator and adjusted by means of the polarization controller (PC).

In the configuration under-study, the dynamics of **S** and **J** are related to the stability of the stationary states of the system, which are the solutions of Eqs.(1) in the CW limit, i.e. when dropping the time derivatives.

In the limit where losses are neglected the stationary states of Eqs.(1) read as [25]:

$$\begin{aligned} \mathbf{S}(z) = {} & [\,\mathbf{S}(0) - \boldsymbol{\Omega}\bullet\mathbf{S}(0)\,\boldsymbol{\Omega}/|\boldsymbol{\Omega}|^2\,]\cos(|\boldsymbol{\Omega}|\,z) \\ & + \boldsymbol{\Omega}\bullet\mathbf{S}(0)\,\boldsymbol{\Omega}/|\boldsymbol{\Omega}|^2 + [\,\boldsymbol{\Omega}\times\mathbf{S}(0)/|\boldsymbol{\Omega}|]\sin(|\boldsymbol{\Omega}|\,z) \end{aligned} \qquad (2)$$

where • indicates the scalar product and $\boldsymbol{\Omega}$=**S**-D**J** is an invariant throughout the fiber. In [25] the following relation is reported which ties the input polarization alignment $\mu = K^{-1}[-\mathrm{D}\mathbf{J}(L)]\bullet\mathbf{S}(0)$ and the output polarization alignment $\eta = K^{-1}[-\mathrm{D}\mathbf{J}(L)]\bullet\mathbf{S}(L)$, being $K = |\mathrm{D}\mathbf{J}||\mathbf{S}|$ a system invariant:

$$\begin{aligned} \mu = {} & (|\mathrm{D}\mathbf{J}|\,\eta + |\mathbf{S}|)\,(|\mathbf{S}|\,\eta + |\mathrm{D}\mathbf{J}|)\,(1-\cos(|\boldsymbol{\Omega}|\,L)) \\ & /(|\mathrm{D}\mathbf{J}|^2 + |\mathbf{S}|^2 + 2K\eta) + \eta\cos(|\boldsymbol{\Omega}|\,L) \end{aligned} \qquad (3)$$

Here we underline that, since $|\mathrm{D}\mathbf{J}| \equiv \gamma(8/9)|\mathbf{J}| \equiv \gamma(8/9)|gR\mathbf{S}|$

$\equiv \gamma(8/9)g|\mathbf{S}|$, then in the limit $g>>1$, Eqs.(3) gives $\mu \simeq \eta$, which gives:

$$\mathbf{s}(L) \bullet D_R \mathbf{s}(L) = \mathbf{s}(0) \bullet D_R \mathbf{s}(L) \qquad (4)$$

The whole of the output stationary SOPs $\mathbf{s}(L)$ solving Eq.(4) describes a closed line over the Poincaré sphere, which we call here Line of Stationary Output SOPs (LSOS) and whose shape depends both on the input $\mathbf{s}(0)$ and on the rotation matrix R.

In ref. [22] a general rule was reported dealing with the stability of these stationary solutions and stating that a stationary solution is stable if it exhibits a non-oscillatory evolution along the whole fiber length. We point out that the vector $\mathbf{S}(z)$ given by Eq.(2) is formed by the three orthogonal components $\mathbf{\Omega}\bullet\mathbf{S}(0)\,\mathbf{\Omega} / |\mathbf{\Omega}|^2$, [$S(0) - \mathbf{\Omega}\bullet\mathbf{S}(0)\,\mathbf{\Omega} / |\mathbf{\Omega}|^2$] $\cos(|\mathbf{\Omega}|z)$ and $[\mathbf{\Omega} \times \mathbf{S}(0) / |\mathbf{\Omega}|] \sin(|\mathbf{\Omega}|z)$ that are all monotonic in z if $|\mathbf{\Omega}|L < \pi/2$. Considering that if $g >> 1$ then $|\mathbf{\Omega}| \equiv |\mathbf{S} - D\mathbf{J}| \simeq |D\mathbf{J}| \equiv \gamma(8/9)g|\mathbf{S}|$, we obtain that a stationary state is stable only if the condition $\gamma g|\mathbf{S}|L<9\pi/16$ is satisfied. We remind that this condition holds as long as fiber losses can be neglected. Note however that our numerical simulations confirm that this condition still holds in presence of weak fiber losses (typically 0.2 dB/km) after substitution of $|\mathbf{S}|$ for $|\mathbf{S}(L)| \equiv P_S(L)$. Actually if $\gamma g P_S(L)L < 9\pi/16$, or equivalently $g<9\pi/(16\cdot L\cdot Ps(L)\cdot\gamma)$, then the stationary states belonging to the LSOS are stable and represent an attraction point on the Poincaré sphere. We thus confirm the existence of an attraction regime that, as already observed in ref. [17], is characterized by an upper threshold g_A here estimated by the relation $g_A = 9\pi / (16\cdot L\cdot Ps(L)\cdot\gamma)$. In this regime, if a CW SOP $\mathbf{s}(0,t) = \mathbf{s}(0)$ is injected into the fiber, then the corresponding output SOP $\mathbf{s}(L,t)$ always converges in time towards a fixed point belonging to the LSOS, which is analogous to the attraction process experienced by $S_1(L,t)$ in Fig.2(a-c).

The position of the point on the LSOS depends on $|\mathbf{\Omega}|L$, and thus on the product $\gamma g P_S(L)$. This means that, by adjusting the value of the amplification factor g, different points on the LSOS can be reached.

On the other hand, when $g > g_A$ the system no longer operates in the attraction regime. More precisely, a threshold g_C is found such that, if $g_A < g < g_C$ the system operates in a transition regime for which the output SOP could reach a constant-in-time value, as well as a periodic, or even a chaotic temporal trajectory. The dynamics of the system is found to depend on both the particular input SOP and the rotation matrix R. Finally, when $g > g_C$, a chaotic regime is reached for which the output SOP trajectory is aperiodic irrespective of the input SOP and the rotation matrix R. This aperiodic behavior favors the coverage of the whole Poincaré sphere and therefore leads to an efficient scrambling of the output SOP. The basic principle of the present polarization scrambling device relies on this particular operating regime. Note that, as will be discussed later, this chaotic dynamics is characterized by the presence of a positive Lyapunov coefficient [17].

Our numerical simulations show that the threshold gain g_C beyond which a chaotic regime occurs is typically in the range of [5-10] g_A. Both g_A and g_C are thus $\propto (L\cdot Ps(L))^{-1} \equiv (L\cdot Ps(0)\cdot\exp(-\alpha L))^{-1}$, therefore for typical propagation losses of about 0.2 dB/km ($\alpha = 0.046$ km^{-1}) and a fiber length $L < 20$ km these thresholds can be reduced by increasing the fiber length.

Let us now illustrate the general system dynamics by considering numerical simulations including the experimental parameters of Fiber-1. These results are reported in Figs. 4 when a $P_S(0) = 15$ dBm CW forward signal is injected into the system.

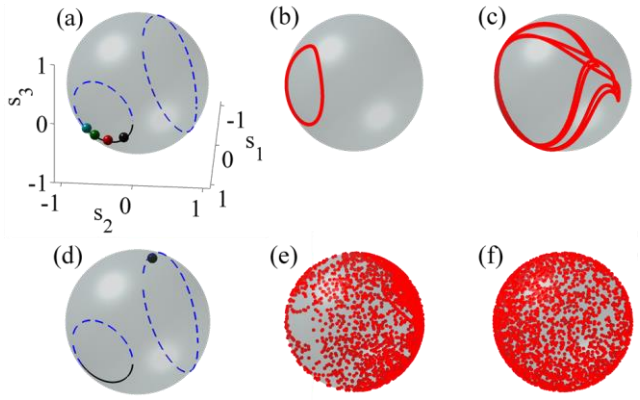

Fig.4 Numerical output distribution of the SOP $s(L,t)$ over the Poincaré sphere for increasing values of the reflective coefficient g . Input power is $P_S(0) = 15$ dBm; fiber is Fiber-1 (L = 5.3 km; losses 0.24 dB/km; $\gamma = 1.7$ W^{-1}km^{-1}). Panel (a): fixed stable points reached by $s(L,t)$ when $g = 2$ (black dot), $g = 4$ (red dot), $g = 6$ (green dot) and $g = 8$ (cyan dot). Panels (b) and (c): periodic trajectories corresponding to $g = 12$ and $g = 16$, respectively. Panel (d): fixed unstable point reached by $\mathbf{s}(L,t)$ when $g = 25$. Panel (e): semi-chaotic trajectory corresponding to $g=28$. Panel (f): chaotic trajectory corresponding to $g = 50$. The closed curves in panels (a, d) form the Line of Stationary Output SOPs (LSOS), which is defined by the equations $\{2\ s_1s_2 + s_3^2 = s_2\ ;\ s_1^2+s_2^2+s_3^2 = 1\}$. The black solid line corresponds to the stable part of the LSOS, composed by the stable stationary states; the blue dotted line corresponds to the unstable part, composed by the unstable stationary states.

For this configuration, $P_S(L) = 13.8$ dBm, and we can thus estimate $g_A = 9\pi/(16\cdot L\cdot Ps(L)\cdot\gamma) \simeq 8$ as well as $g_C \simeq 5g_A \equiv 40$. For this series of simulations, the SOP of the input signal is aligned with the x-axis of the Poincaré sphere, that is to say $\mathbf{s}(0,t) = \mathbf{s}(0) = (1,0,0)$ and $R = [(0,1,0); (-1,0,0); (0,0,1)]$. In this case, Eq.(4) reads as $2\ s_{L1}\ s_{L2} + s_{L3}^2 = s_{L2}$, where $s_{L1,2,3}$ are the components of $\mathbf{s}(L)$ and are subject to the constraint $|\mathbf{s}|^2 \equiv s_{L1}^2+s_{L2}^2+s_{L3}^2 = 1$. The corresponding LSOS, formed by two closed and distinct curves over the Poincaré sphere, are plotted in Fig. 4a, where both the stable (black solid line) and the unstable part (blue dashed line) of the LSOS are put in evidence.

Fig. 4a illustrates the attraction regime, i.e. when $g<g_A$. It displays the fixed points that are reached by the output SOP when $g = 2$ (black dot), $g = 4$ (red dot), $g = 6$ (green dot) and $g = 8$ (cyan dot), respectively. As predicted theoretically, a unique deterministic point is reached for each value of g and more importantly, this point lies on the stable part of the LSOS. Figures 4(b-e) illustrate the transition regime, that is to say when $g_A < g < g_C$. As previously mentioned, more or less complex periodic trajectories can be observed in this regime, for instance in panel (b) for $g = 12$ and in panel (c) for $g = 16$,

as well as fixed unstable points (panel (d), g = 25). Indeed, our numerical simulations reveal that if a fixed point is reached in the transition regime, then it always belongs to the unstable part of the LSOS. For this reason, even a small perturbation of the system parameters, for example of the coefficient g or of the rotation matrix R, leads to a dramatic change in the output dynamics of $\mathbf{s}(L,t)$, which can evolve towards a complex periodic or semi-chaotic trajectory. This feature is clearly visualized in panels (d) and (e), corresponding to a variation of the amplification factor from $g = 25$ to $g = 28$.

The semi-chaotic trajectory in Fig. 4(e) is the signature of the transition from the transient regime to the chaotic regime: the path of $\mathbf{s}(L,t)$ over the Poincaré sphere exhibits an apparent random motion, although it only fills a part of the surface of the Poincaré sphere. In the chaotic regime ($g > g_C$, panel (f)) the trajectory is well distributed all over the surface of the Poincaré sphere, so that an efficient and nondeterministic polarization scrambling of the output signal is achieved, in agreement with our predictions. Obviously, this is the ideal operating regime for the present all-optical polarization scrambler.

V. Experimental Results

In order to confirm our numerical predictions, a series of experiments have been carried out by means of Fiber-1. To this aim, a 100-GHz incoherent signal was injected into the system with a fixed and arbitrary polarization state as well as a constant average power $P_S(0) = 15$ dBm.

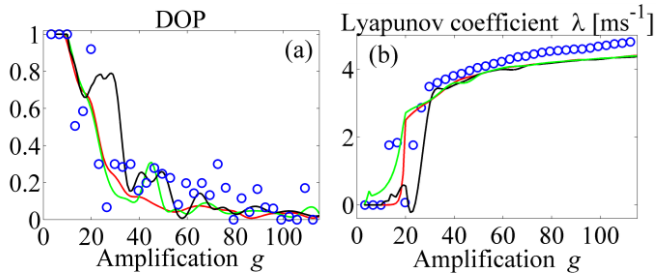

Fig. 5 DOP (a) and Lyapunov coefficient (b) of the output signal as a function of the reflective coefficient g. The input power is $P_S(0)$=15 dBm; fiber is Fiber-1 (L=5.3 km; losses 0.24 dB/km; γ=1.7 $W^{-1}km^{-1}$).The blue circles correspond to the experimental measurements. The DOP close to the unity around g=20 corresponds to the attraction towards an unstable stationary states in the transient regime. Color solid lines display the results of numerical simulations for 3 particular rotation matrices R and 3 different input conditions of the SOP.

The performance of our all-optical polarization scrambler was first experimentally characterized by evaluating the degree of polarization (DOP) as a function of the backward power, i.e. the amplification coefficient g. The DOP is classically defined as $DOP = (\langle s_{L1}\rangle^2 + \langle s_{L2}\rangle^2 + \langle s_{L3}\rangle^2)^{1/2}$ and is used to quantify the scrambling efficiency of the output SOP $\mathbf{s}(L,t)$ over the Poincaré sphere. As it can be seen in Fig. 5a (blue circles), the DOP of the output signal has initially a value close to unity, which is related to the constant-in-time output SOP that characterizes the attraction regime.

The DOP starts to decrease beyond the amplification threshold $g \simeq 8$, in perfect agreement with our prediction of g_A. When $g > 8$, the system enters in the transient regime. In such a regime small variations of the amplification g could give rise to different temporal trajectories of the output SOP that cover only partially (see Fig. 4b) or almost entirely (see Fig. 4e) the Poincaré sphere. For this reason some fluctuations can be observed in the DOP evolution.

Finally, for high values of g, typically above $g_c = 5g_A = 40$, the system enters into the chaotic scrambling regime. The experimental DOP remains lower than 0.3, which corresponds to an efficient scrambling of the output SOP all over the Poincaré sphere. In particular, each sequence of S_1, S_2 and S_3 is characterized by autocorrelations that rapidly tend to zero, indicating that they don't exhibit deterministic repetitive patterns, in agreement with our numerical predictions. We stress here the fact that in this regime the Lyapunov coefficient $\lambda(z = L)$ is always positive (Fig. 5b), which provides a key signature of the chaotic nature of the dynamics of the output SOP.

Moreover, it is important to note that, contrary to the transition regime, in the chaotic regime the output SOP dynamics is almost independent of the input SOP or rotation matrix R. Indeed a variation of these two parameters simply produces a different aperiodic trajectory of the output SOP. For this reason in Fig. 5 when $g > g_C$, no major difference between the 3 solid curves can be observed, that refer to the numerical solutions of Eqs. 1 with 3 different input SOPs and matrix R randomly chosen. The system also becomes independent of the input power, but in practice we have observed that the more the input power is, the easier the system enters into the chaotic regime. In fact, when the device operates with moderate powers, an adjustment of the polarization controller PC is needed in order to force the system to evolve into an unstable chaotic region.

In addition we have also checked that, for typical values of power used in these experiments, no polarization scrambling occurs if the counter-propagating beam is an external wave generated independently of the forward wave [26, 27]. This

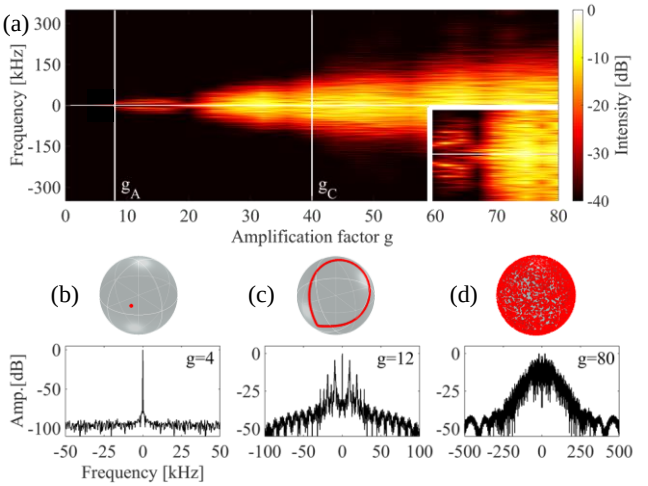

Fig. 6 (a) Experimental RF spectrum of the output component S_1 as a function of the amplification factor g. The input power is $P_S(0)$ = 15 dBm; fiber is Fiber-1 (L = 5.3 km; losses 0.24 dB/km; γ = 1.7 $W^{-1}km^{-1}$).The inset shows a magnification of the spectrum between g_A et g_C. Snapshots (b), (c) and (d) illustrate the spectrum of S_1 and the output SOP distribution on the Poincaré sphere when the backward power is 20 dBm (g = 4), 25 dBm (g = 12) and 33 dBm (g = 80), respectively.

clearly indicates that the instability of the system is in fact fundamentally related to the feedback effect imposed by the reflected loop setup.

The dynamics of the system is even more striking when characterized in the spectral domain. For that purpose, we have measured the RF spectrum of the output Stokes component S_1. These measurements were achieved by recording the electrical RF spectrum of the temporal intensity profile detected behind an optical polarizer.

Fig. 6a displays the evolution of the output RF spectrum as a function of the backward power $P_J(L) = gP_S(L)$ and the corresponding g parameter. The 3 regimes previously discussed are distinctly visible:

- When $P_J(L) < 23$ dBm ($g < g_A = 8$), the system is in the attraction regime: the spectrum always exhibits a single narrow peak centered in f = 0 Hz, which corresponds to a constant-in-time value in the temporal domain and thus a constant output SOP.

- When 23 dBm $< P_J(L) < 30$ dBm ($8 < g < 40$), the transition regime is reached, and as previously mentioned the system can exhibit 3 different dynamics: either an attraction towards an unstable stationary point, which corresponds to a DOP close to the unity (see in Fig. 5 the experimental results for $g \simeq 20$) and to a narrow peak in the RF spectrum; either a periodic trajectory, which corresponds to equally spaced narrow peaks in the RF spectrum; or a semi-chaotic trajectory for which the RF spectrum begins to broaden.

- Finally in the chaotic regime, for $P_J(L) > 30$ dBm ($g > 40$) the spectrum evolves in a much broader continuum of frequencies without showing any discrete component, which corresponds to an increasing scrambling speed and true chaotic behavior of the output polarization.

The snapshots (b-d) in Fig. 6 and corresponding Poincaré spheres illustrate the 3 typical regimes of our scrambler. Snapshot (b) for $P_J(L) = 20$ dBm (g=4) depicts the attraction regime, characterized by a single peak centered in f = 0 Hz in the RF spectrum of S_1. For $P_J(L) = 25$ dBm ($g = 12$), the snapshot (c) shows the transient regime: discrete frequency harmonic components in the RF spectrum are localized at n×13 kHz, corresponding to a closed and periodic trajectory on the Poincaré sphere. Finally, snapshot (d) reports an example of the chaotic regime for $P_J(L) = 33$ dBm ($g = 80 > g_c$); we can clearly see a continuum of frequencies in the RF spectrum, corresponding to an almost uniform coverage of the Poincaré sphere and thus an efficient polarization scrambling of the output signal.

Note in this respect that a theoretical description of the spectral dynamics of the Stokes components in this chaotic regime of the polarization scrambler is in progress by making use of the wave turbulence theory [28].

Furthermore, as shown in Fig.7, in the chaotic regime all the normalized Stokes parameters exhibit a nearly uniform probability density function, which provides further evidence of the polarization randomization. Note that a perfectly uniform density function of the Stokes components would correspond to a DOP close to 0, whereas in our case the non-perfect uniformity entails a DOP > 0, but always lower than 0.2 for large values of g (see Fig.5a).

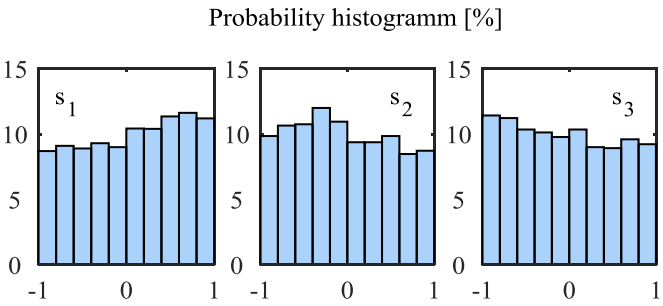

Fig. 7 :Experimental probability histogram ([%]) of the 3 normalized Stokes parameters s_1, s_2 and s_3. The input power is $P_S(0) = 15$ dBm; the backward power is $P_J(L) = 33$dBm; the fiber under test is Fiber-1 (L = 5.3 km; losses 0.24 dB/km; $\gamma = 1.7$ W^{-1}km^{-1}). The corresponding Poincaré sphere is represented in Fig. 6(d).

Our home-made polarization scrambler was also tested for Telecom applications. In particular, we have characterized the signal degradation due to the nonlinear regime occurring during the propagation. The initial incoherent signal was thus replaced by a 10-Gbit/s OOK signal centered at 1550-nm. The input SOP was kept constant and the injected power in Fiber-1 was fixed to $Ps(0) = 15$ dBm. Figure 8a displays the output Poincaré sphere of the 10-Gbit/s signal for a backward power of 30 dBm ($g \simeq 40$). It corresponds to an experimental scrambling speed of 107 krad/s and thus confirms that an efficient scrambling process can be achieved, even with high-repetition rate modulated signals. Moreover, Fig. 8b shows that the shape of the pulses is also remarkably preserved with a wide-open output eye-diagram, which validates the applicability of our polarization scrambler for RZ modulated signals.

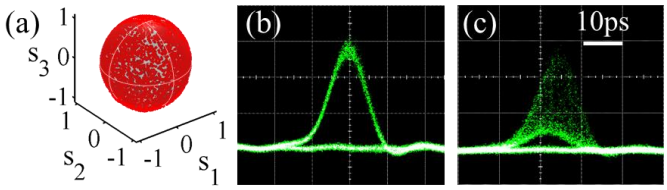

Fig. 8 Poincaré sphere (a) and eye-diagram (b) of the 10-Gbit/s signal recorded at the output of Fiber-1 (L = 5.3 km; losses 0.24 dB/km; $\gamma = 1.7$ W^{-1}km^{-1}) for an input average power of 15 dBm and a backward power of 30 dBm. Panel (c): output eye-diagram for a backward power of 35 dBm.

Finally, due to its intrinsic principle, the main limitation of our system is the strong Rayleigh back-scattering generated from the high power counter-propagating replica. In fact, the Rayleigh emission is coupled to the scrambled signal through the output circulator, which induces a non-negligible amount of noise at the signal frequency. This phenomenon is well illustrated in Fig. 8c, where the backward power is increased up to 35 dBm ($g \simeq 120$). The corresponding output eye-diagram turns dramatically closed with a high level of amplitude jitter. As a consequence, this deleterious effect limits the maximum backward power that can be re-injected into the fiber and thus the scrambling speed that can be achieved. A practical solution to limit this drawback would be to use a frequency offset pump channel which first copropagates with the initial signal but still

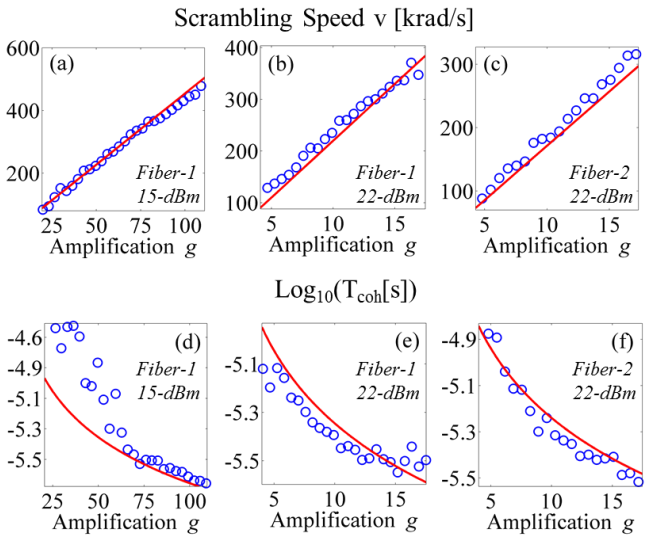

Fig. 9 Experimental measurements (blue circles) and analytical estimations by means of Eqs.(7-8) (red solid line) of the scrambling speed and coherence time (in logarithmic scale). Fibers under test are Fiber-1 (L = 5.3 km; losses 0.24 dB/km , i.e. $\alpha = 0.055$ km^{-1}; $\gamma = 1.7$ W^{-1}km^{-1}) and Fiber-2(L = 10 km; losses 0.2 dB/km, i.e. $\alpha = 0.046$ km^{-1}; $\gamma = 1.7$ W^{-1}km^{-1}).
Two different input powers Ps(0) have been used: 15 dBm and 22 dBm. Panels (a,d): case of Fiber-1 and input power 15 dBm (for which $g_C \simeq 40$) ; panels (b,e): case of Fiber-1 and input power 22 dBm ($g_C \simeq 8$); panels (c,f): case of Fiber-2 and input power 22 dBm ($g_C \simeq 6$).

remains the only back-reflected beam. This technique has been implemented in the last section of the paper for the WDM configuration.

VI. Scrambling Performances

In this section we analyze the performances of our device in terms of scrambling speed and coherence time. The scrambling speed *v* represents the average angle covered by **s** in 1 second over the Poincaré sphere:

$$v = Lim_{\partial t \to 0} \left\langle |\partial \mathbf{s}| / \partial t \right\rangle \qquad (5)$$

where, in the limit $\partial t \to 0$, the dimensionless quantity $|\partial \mathbf{s}| = |\mathbf{s}(t+\partial t) - \mathbf{s}(t)|$ represents the angle between the two vectors $\mathbf{s}(t+\partial t)$ and $\mathbf{s}(t)$ over the unitary Poincaré sphere and can therefore be expressed in dimensionless units of radians. Consequently, we will indicate the speed in units of rad/s.

The output coherence time is defined as $T_{coh} = (t_{c1}+t_{c2}+t_{c3})/3$, being t_{ci} (i={1,2,3}) the coherence time related to the component s_{Li}, that is the area of the associated auto-correlation function [29]:

$$t_{ci} = \int_{\tau=-\infty}^{\infty} \left\langle s_{Li}(t+\tau) \cdot s_{Li}(t) \right\rangle \qquad (6)$$

This parameter reveals how fast the polarization fluctuations of the output SOP become uncorrelated, and is thus an important quantitative index to evaluate how quickly the depolarization process occurs.

In order to derive a design rule of the output scrambling speed as a function of the system parameters, we have fitted our previous numerical results by means of a least-square interpolation, using as model function $v_m = k_1 \gamma g P_S(0) \exp(-k_2 \alpha L)$. The best fit to the numerical data is provided by $k_1 = 4c_0/9$, where c_0 is the speed of light in the vacuum, and $k_2 = 5/3$. Furthermore, we found that the output coherence time is well interpolated by $1/v$, which leads to the estimations:

$$v = (4/9) c_0 \, \gamma \, g P_S(0) \exp(-5\alpha z/3) \qquad (7)$$

$$T_{coh} = (9/4)(c_0 \, \gamma \, g P_S(0))^{-1} \exp(5\alpha z/3) \qquad (8)$$

The validity of these estimations is illustrated in Fig. 9, where the scrambling speed and the coherence time calculated by means of Eqs. (7-8) are in excellent agreement with the experimental measurements obtained thanks to the 100-GHz incoherent signal and both Fiber-1 and Fiber-2. Eqs. (7-8) and results reported in Fig. 9 confirm the tendency previously observed in ref. [17], that is to say that in the chaotic regime the scrambling speed grows up linearly with *g*. This confirms that *g* is the key parameter to control the temporal fluctuations of the output polarization. The scrambling speed reaches some hundreds of krad/s. Although this value is smaller than those of commercially available devices, it makes our chaotic scrambler of practical interest for the testing of real fiber optic systems. Note also that by increasing the fiber length, one can reduce the thresholds g_A and g_C. However, the drawback is that this solution increases the total propagation losses, which degrades the scrambling performances and sets therefore a limit on the maximum fiber length *L*.

VII. Cascade of Scramblers

In order to overcome the limits imposed on the fiber length and on the backward power, discussed in the previous sections, we may take advantage of higher Kerr nonlinearities, e.g., in bismuth, tellurite, chalcogenide fibers, or more generally in soft-glass fibers [30, 31, 32], so as to make our polarization scrambler faster and compact. A different approach consists in implementing a cascade of scramblers where the forward beam **S** exiting the n^{th}-scrambler is amplified at its original power and then injected in the $(n+1)^{th}$-scrambler as illustrated in Fig. 10. Such a configuration is more complex and expensive than the single scrambler and other cascade systems already proposed in literature [33]. On the other hand, it would allow limiting both the fiber length and the backward power at each stage, in such a way that propagation losses and back Rayleigh scattering remain negligible. On the other hand, the complexity of the cascade setup is proportional to the number of scramblers, which practically puts a limit on the maximum number of stages. However, contrary to a concatenation of classical linear polarization manipulations with well-defined eigenstates, which usually impose a succession of deterministic rotations and thus are enable to produce highly chaotic depolarized light, here we exploit a nonlinear process between counter-propagating waves, which is known to induce high polarization instabilities [20-21]. More precisely, the principle of operation of our cascade of scramblers relies on the fact that, as any chaotic system, a small perturbation of the input parameters will induce a dramatic change in output. This butterfly effect,

intrinsic to the Omnipolarizer, will manifest here as a completely different trajectory on the output Poincaré sphere. The cascade of scramblers exploits this property that the more unstable in time the input SOP is, the more efficient our polarization scrambler is with moderate powers. Consequently, the first polarization scrambler of the cascade will induce a periodic or quasi-periodic perturbation of the input SOP, while the following scramblers will extend the genuine nature of the output SOP, then characterized by an increasing Lyapunov coefficient.

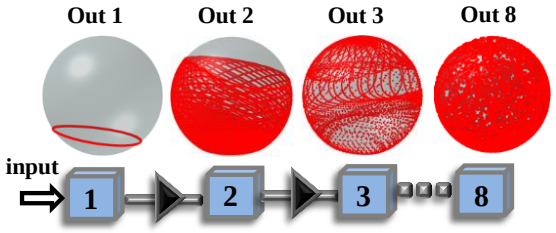

Fig. 10 Representation of the sequential cascade of 8 scramblers. See text for details on system parameters. The cyan numbered boxes identify the scramblers in the cascade; the black triangles indicate the re-amplification of the forward signal between two consecutive scramblers. The output SOP at the exit of the scramblers in the cascade is plotted over the Poincaré sphere when the amplification is set to $g = 12$ in each scrambler.

Indeed, we can notice that if the input SOP to a single scrambler is not constant-in-time (CIT), then its chaotic amplification threshold is reduced, i.e. we have a new threshold $g_C' < g_C$, being g_C the threshold in presence of a CIT input SOP. Furthermore, we observe that the higher the scrambling speed of the input SOP, the lower this new threshold g_C' is, and that the scrambling speed of the output SOP is larger than the speed related to the input SOP.

Let us now consider a cascade of N stages where each scrambler is characterized by an amplification $g > g_A$ and where the input SOP at the 1st scrambler is CIT. Being $g > g_A$, the SOP at the output of the 1st scrambler typically follows a periodic or aperiodic trajectory, thus it is non-CIT. As a consequence of the aforementioned observation, the threshold $g_C^{(2)}$ related to the 2nd scrambler will be lowered, i.e. $g_C^{(2)} < g_C$, and the scrambling speed at the output of the 2nd scrambler will be larger than the speed at the output of the 1st scrambler.

Extending this reasoning to the whole cascade, we find that the scrambling speed is improved at the output of each stage, whereas the chaotic threshold is reduced. If the threshold $g_C^{(N)}$ related to the last scrambler of the cascade is $g_C^{(N)} < g$, then we observe a chaotic SOP at the output of the cascade, and thus an efficient scrambling over the Poincaré sphere. Being that the chaotic threshold is reduced at each stage, in a cascade with lots of scramblers the condition $g_C^{(N)} < g$ can be reached even when the amplification g is only slightly larger than g_A. Therefore, when plotting the output DOP as function of g, we envisage a sharp cut-off in proximity of g_A: indeed whenever $g > g_A$ the SOP at the exit of the cascade will be chaotic and well scrambled (i.e. DOP ≈ 0). On the contrary, when $g < g_A$ each scrambler of the cascade works in the attraction regime, so that the corresponding output SOP, after a short transient time, is attracted towards the LSOS. As a consequence, the DOP at the output of the cascade is nearly unitary.

In Fig. 10 the distribution over the Poincaré sphere of the SOP **s** at the output of the stages in a cascade of 8 scramblers is displayed. The fiber implemented in each scrambler is Fiber-1 (L = 5.3 km), thus the total length of the cascade system is $L_{cascade}$ = 42.4 km. The power $P_s(0)$ injected in the cascade is 15 dBm, and is kept constant at the input of each stage thanks to the re-amplification of the forward signal between two consecutive scramblers. Therefore $g_A \simeq 8$ for any scrambler of the cascade. The amplification gain g is set to 12 at each stage. In this configuration the SOP **s**, which follows a simple periodic trajectory at the output of the first scrambler (Out 1 in Fig. 10), becomes more and more scrambled and chaotic at the output of the following scramblers.

It is important to highlight that if a unique scrambler with a fiber length $L_{cascade}$ were employed then the scrambling performances would be completely degraded by losses (see Eqs (7,8)). Despite losses, the implementation of the cascade process enable to achieve much faster polarization fluctuations. In Fig. 11, for the cascade depicted in Fig. 10, we show the numerical calculation of both the DOP and the scrambling speed at the output of consecutive stages as a function of the amplification g.

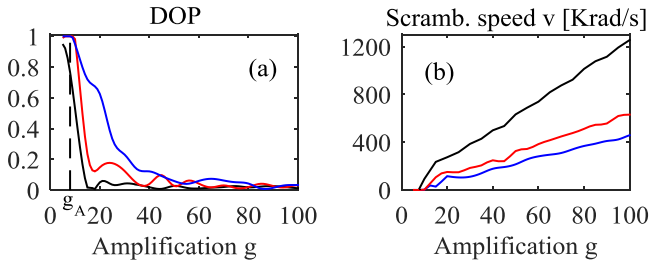

Fig. 11 Degree of polarization (DOP) and scrambling speed v of the output SOP at the exit of the 1st scrambler (blue line), 2nd scrambler (red line) and 8th scrambler of the cascade that is represented in Fig.9. The amplification g is the same at each stage. The black dotted vertical line indicates the cut-off g_A for the DOP at the exit of cascade.

We note that the scrambling speed is strongly improved at each stage, and that at the exit of the 8th stage the speed is increased up to three times with respect to the output of the 1st scrambler. Furthermore, the DOP becomes lower at each stage, which indicates a uniform coverage of the whole Poincaré sphere at the exit of the cascade even with a low amplification gain g. Moreover, our numerical results reveal that this scrambling process is accompanied by an increase of the Lyapunov coefficient at each stage of the cascade. Indeed, starting close to zero at the output of the 1st scrambler, the Lyapunov coefficient always remains positive and largely increases with the number of scramblers N, which proves the chaotic nature of this process. In addition, a sharp cut-off in proximity of g_A is observed in the DOP function related to the exit of the last scrambler (see black line in Fig. 11a), so that if $g < g_A$ then the DOP is close to unity, while if $g > g_A$ then the DOP is close to zero. This suggests that in a cascade configuration where lots of scramblers are implemented, the chaotic threshold is reduced down to nearly g_A, that is to say $g_{C,cascade} \simeq g_A$. Finally, the cascade allows for a considerable increment of the scrambling speed: we expect that by implementing a cascade of scramblers with highly-nonlinear fibers, e.g. $\gamma > 10$ W^{-1}km^{-1}), a speed of some Mrad/s could be reached.

VIII. WDM CAPABILITIES

In this section we experimentally characterize the behavior of our all-optical scrambler in the context of a WDM transmission. To this aim, we have implemented the experimental setup depicted in Fig.12.

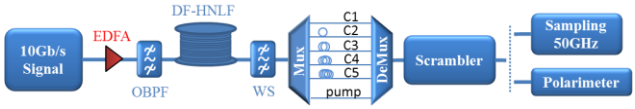

Fig. 12 Experimental setup for testing the chaotic polarization scrambler in WDM configuration. WS: Waveshaper.

The initial signal first consists in a train of 10-GHz pulses generated from a mode-locked fiber laser (MLFL) at 1551 nm with 2-ps full width at half maximum (FWHM). The pulses are encoded at 10 Gbit/s in the OOK modulation format using a 2^{31}-1 pseudo-random binary sequence (PRBS). The resulting data signal is then amplified to 30 dBm by means of an EDFA and injected into a 500-m long dispersion-flattened highly non-linear fiber (DF-HNLF from *ofs*) in order to broaden the spectrum thanks to self-phase modulation and associated wave-breaking phenomenon [34]. The DF-HNLF is characterized by a chromatic dispersion of –1 ps/nm/km at 1550 nm, a dispersion slope of 0.006 ps²/nm/km, fiber losses of 0.6 dB/km and a nonlinear Kerr coefficient of 10.5 $W^{-1}.km^{-1}$. The resulting continuum is then sliced into five 10-Gbit/s OOK WDM channels and an additional pump channel by means of a programmable optical filter (Waveshaper WS). As illustrated in Fig. 13, which shows the experimental continuum recorded at the output of the HNLF and the resulting spectral grid, our final WDM signal consists in 5, 10-Gbit/s, 100-GHz spaced, 12-GHz bandwidth channels centered respectively at 1540.2 (C1), 1542 (C2), 1543.45 (C3), 1545(C4) and 1546.2 nm (C5), as well as a pump channel centered at 1550 nm.

All the WDM channels are then decorrelated in time and polarization domains thanks to a combination of two optical demultiplexer/multiplexer with different delay-lines and polarization rotations for each channel before injection into our optical scrambler. As in the single-channel experiment described above, the 10-Gbit/s WDM signals are then injected into the system with a constant total average power of 15 dBm (7 dBm/channel). It is here important to notice that a 100 GHz optical bandpass filter was added into the reflective-loop so as to only keep the pump channel at 1550 nm for the backward signal, whilst the 5 other WDM channels are characterized at output of the device. The role of this spectral manipulation is twofold: on the one hand, it ensures a unique state-of-polarization for the counter-propagating signal in order to maximize the efficiency of the scrambling process for all the transmitted channels. On the other hand it limits the deleterious impact of back Rayleigh scattering on the 5 other transmitted channels. At the output of the system, the 5 WDM channels were demultiplexed and individually characterized in polarization as well as in the temporal domain by means of eye-diagram monitoring and bit-error-rate measurements.

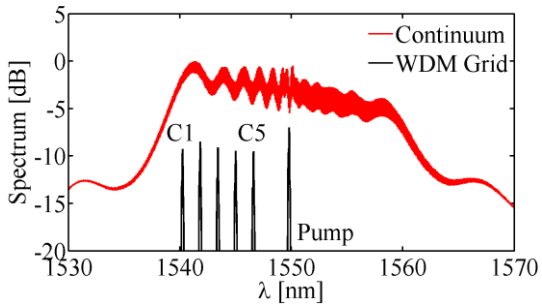

Fig. 13. Experimental continuum recorded at the output of the DF-HNLF for an input power of 30 dBm (red). 10-Gbit/s WDM grid obtained by spectral slicing (black solid line).

Figures 14(a-c) display the Poincaré spheres of the different WDM channels recorded at the output of the all-optical scrambler. To not overload the paper, we report only 3 (among 5) Poincaré spheres, which correspond to C1: 1540.2 nm, C3: 1543.45 nm and C5: 1546.2 nm WDM channels, respectively; the 2 other channels exhibit similar performances. For this series of measurements, the total input power is kept constant to 15 dBm while only the 1550-nm pump channel is reflected and amplified in the backward direction with an average power of 29 dBm.

Quite remarkably, we can first notice that despite the 5 input channels are initially uncorrelated in such a way that each of them enters into the system with a different and unique SOP, the device is able to scramble the whole WDM grid. Indeed, in Fig.14 each individual channel covers the whole surface of the Poincaré sphere and is characterized by a low value of its DOP, close to 0.2 for each channel.

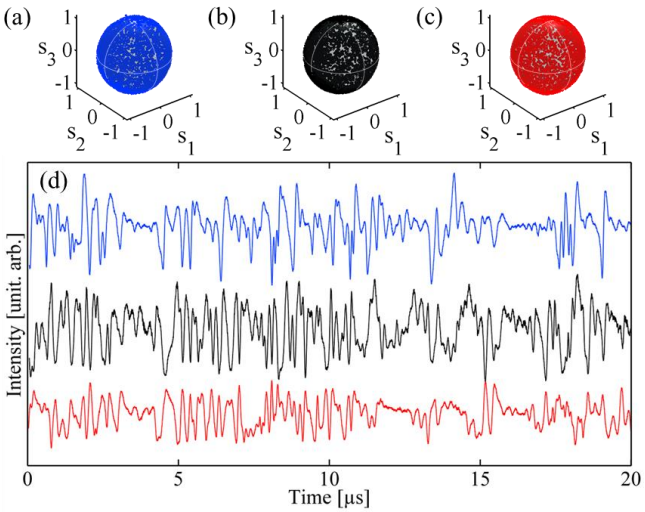

Fig. 14 (a-c) Output Poincaré spheres for WDM channels C1, C3 and C5, respectively. The input power is fixed to 15 dBm while the reflected 1550-nm pump channel is amplified to 29 dBm. (d) Intensity of the 3 output channels C1, C3 and C5 recorded behind a polarizer by means of a low bandwidth photodetector and oscilloscope.

It is also interesting to note that, at the output of the device, all the random SOP trajectories undergone by the 5 different WDM channels are in fact correlated in time and are characterized by the same scrambling speed, close to 130 krad/s, see Table 1, in good agreement with numerical

simulations. It is also important to notice that the scrambling speeds raised by all the WDM channels are roughly the same than the one measured in the previous single channel experiment. Indeed, this all-optical scrambler is mainly sensitive to the average power of the counter-propagative beam.

Table 1: Scrambling speed (krad/s)

Channels (nm)	C1 1540.2	C2 1542	C3 1543.45	C4 1545	C5 1546.2
Experiments	156	120	132	112	114
Numerics	143	142	139	143	144

The time-correlation of the channels SOPs is also highlighted in Fig. 14d in which the intensity profiles of the 3 demultiplexed output WDM channels C1, C3 and C5 are synchronously recorded behind a polarizer by means of a low bandwidth photodetector and an oscilloscope. One can clearly notice the temporal correlation of polarization fluctuations between the different channels. This unexpected behavior can be intuitively interpreted considering the fact that only one pump channel is back reflected. Therefore, this pump channel imposes the polarization random walk over the Poincaré sphere for all the other channels, as well as their scrambling speed.

The impact of the nonlinear polarization scrambling process on the 10-Gbit/s temporal profiles is illustrated in Fig. 15 for the WDM channels C1, C3 and C5. The two other channels have similar behavior. The upper row of insets underlines the high quality of the transmitted eye-diagrams obtained at the output of the fiber in passive configuration, i.e. when the backward 1550-nm pump channel is switched off. Note that in the WDM configuration the scrambling speeds are comparable with those of the single-channel configuration, but without increasing the total injected power at the input of the system. This fact allows limiting the deleterious impacts of both self-phase and cross-phase modulation. The bottom row shows the corresponding eye-diagrams when the backward pump channel is now switched on at an average power of 29 dBm, so that the scrambling process now operates efficiently.

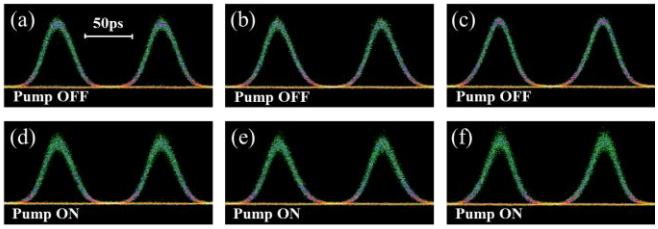

Fig. 15 (a-c) Output eye-diagrams in passive configuration (pump off) for WDM channels C1, C3 and C5, respectively; the input power is fixed to 15 dBm. (d-f) Corresponding eye-diagrams when the backward 1550-nm pump channel is amplified to 29 dBm.

Despite the high quality and wide-open eye-diagrams recorded after the scrambling process, one can however observe a slight degradation of the temporal profiles with an increase of the amount of amplitude jitter. We attribute these impairments to the Rayleigh back-scattering provided by the spectrally broadened backward pump channel as well as a weak Raman depletion effect induced by the pump on the signal. The impairments induced by the scrambling process over the 5 WDM 10-Gbit/s channels have then been quantified by means of systematic bit-error-rate measurements (BER) as a function of the received power in passive (pump OFF) and active (pump ON) configurations, respectively. Note that in the present context, especially to better quantify the impairments induced by back-Rayleigh-scattering over the transmitted signal, BER measurements as a function of optical-signal-to-noise ratio would have been more rigorous than versus received optical power. Especially, because the spectrum of the WDM grid is spread over 6 nm, the amount of noise introduced by the high-power EDFA is not equal for each channel and thus participates differently in each channel penalties. Nonetheless, these proof-of-principle measurements provide a clear signature that our all-optical scrambler does not significantly impair the transmitted signal. Results for the 5 WDM channels are summarized in Fig. 16 and show that a very weak power penalty is provided by the nonlinear scrambling process when comparing Pump ON/Pump OFF configurations. More precisely, a power penalty of 0.2 dB for the whole channels has been measured in average at the BER value of 10^{-9}.

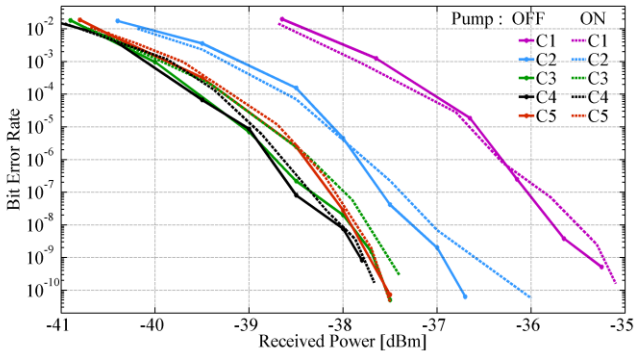

Fig. 16 Bit-error-rate measurements for the 5 WDM 10-Gbit/s channels recorded at the output of the nonlinear scrambler in passive configuration (pump off, solid lines) and in scrambling regime (pump on, circles). The input power is fixed to 15 dBm and the backward pump channel is set to 29 dBm.

Discussion and Conclusions

In this work we have reported a numerical and experimental description of an all-optical, fully chaotic nonlinear polarization scrambler. The basic principle of this device was initially proposed in ref. [17]. It is based on the nonlinear cross-polarization interaction in a standard optical fiber between a forward signal and its high-power counter-propagating replica, generated and amplified by a factor g at fiber end by means of a reflective loop setup. This system is in fact an extension of the device called Omnipolarizer [18] to a new chaotic operating regime. We gain here a deeper understanding of the physics underlying this all-optical scrambler. Indeed, based on numerical simulations, we derive some useful expressions for both the thresholds g_A and g_C that rule the transition between the different operating regimes of the device, as well as a direct estimation of the scrambling speed and the coherence time of the output polarization evolution. These estimations are fully confirmed by experimental results, which draw the attention to

the main factors that limit the scrambling performances.

In particular, experimental results obtained on a 10-Gbit/s OOK signal show that in a Telecom context our device is mainly limited by propagation losses and the detrimental Rayleigh back-scattering when large amplification factors *g* are implemented. These deleterious effects thus limit the scrambling speed of our system around 500 krad/s.

However, to overcome these drawbacks, another scenario has been also proposed and numerically studied which is based on a cascade of chaotic scramblers. This cascade of fibered scramblers allows to obtain an effective scrambling of the polarization even in presence of a relatively small amplification gain *g*, and could noticeably increase the output scrambling speed up to some Mrad/s but unfortunately, at the expense of the global complexity and cost efficiency.

Finally this nonlinear polarization scrambler has been also successfully tested in a 10-Gbit/s OOK WDM configuration. In particular, we have experimentally shown that this device is able to simultaneously scramble the polarization of 5 WDM channels and more surprisingly, despite its chaotic nature, it can impose a time-correlated random walk over the Poincaré sphere for each individual channel at an average speed close to 130 krad/s.

Despite the fact that it appears difficult to compare the performances of well-established commercially available solutions and the present results obtained in the initial stage of a fundamental research, here we think interesting to highlight the main advantages and drawbacks of our all-optical scrambler over existing solutions as well as to highlight some possible ways of improvement.

First of all, if we take into account the whole experimental setup involved to achieve an efficient and fast scrambling process, namely two high-power amplifiers, a few-km long fiber spool, a band-pass filter and optical circulators, clearly commercial units are less expensive and benefit from a significantly lower power consumption (typically 10 W compare to 25 W for the present solution, respectively).

Moreover, the behavior of opto-electronic devices is deterministic, which means that the degree of depolarization as well as the statistical distribution of the output polarization state can be simply controlled and adjusted by applying an appropriate driving current (even chaotic), which allows generating higher scrambling speeds as well as lower values of DOP, see refs [11-13]. In the present solution, the scrambling process is chaotic and only the scrambling speed can be adjusted by means of the backward power. Furthermore, the device is mainly limited by the inherent back-Rayleigh-scattering generated from the counter-propagating pump beam over the output signal. Indeed, even if we have proposed an efficient strategy to overcome and mitigate this drawback by implementing an offset filtering pump channel, the back-Rayleigh-scattering clearly limits the scrambling speed which can be achieved by our device.

Nevertheless, this first fundamental demonstration has the benefit to propose an alternative approach, entirely based on a light-by-light interaction, which could be of a high interest for the development of all-optical technologies in view of future transparent networks.

Moreover, the scrambling speed as well as the power consumption and compactness could be greatly improved by implementing this technology in ultra-high nonlinear materials and high-confinement waveguides such as microstructured soft-glass optical fibers (chalcogenide or tellurite) [30-32] or silicon waveguide integrated on a CMOS compatible chip [35, 36].

To conclude, this home-made device, essentially based on standard components usually available in many Labs working in the field of nonlinear optics and optical communications, opens the path to the concept of fast and truly chaotic all-optical scrambling devices.

ACKNOWLEDGEMENTS

This research was funded by the European Research Council under Grant Agreement 306633, ERC PETAL. https://www.facebook.com/petal.inside. We also thank the financial support of the Conseil Régional de Bourgogne through the Photcom project. We thank Doc. S. Pitois for fruitful discussions.

REFERENCES

[1] F. Bruyere, O. Audouin, V. Letellier, G. Bassie and P. Marmier, "Demonstration of an optimal polarization scramlber for long-haul optical amplifier systems," *IEEE Phot. Technol. Letters*, vol. 6, pp. 1153-1155, 1994.

[2] N. Bergano, V. .Mazurczyk and C. Davidson, "Polarization scrambling improves SNR performance in a chain of EDFAs," in *Proc. of Optical Fiber Commun. Conference*, San José, USA, 1994.

[3] Z. Li, J. Mo, Y. Wang and C. Lu, "Experimental evaluation of the effect of polarization scrambling speed on the performance of PMD mitigation using FEC," in *Proc. of Optical Fiber Commun. Conference 2004*, Los Angeles, USA, 2004.

[4] P. M. Krummrich and K. Kotten, "Extremely fast (microsecond scale) polarization changes in high speed long hail WDM transmission systems," in *Proc. of Optical Fiber Commun. Conference*, Los Angeles, USA, 2004.

[5] B. Koch, R. Noé, V. Mirvoda and D. and Sandel, "100-krad/s endless polarisation tracking with miniaturised module card," *Electron. Lett.*, vol. 47, pp. 813-814, 2011.

[6] W. H. J. Aarts and G. Khoe, "New endless polarization control method using three fiber squeezers," *J. Lightwave Technol.*, vol. 7, pp. 1033-1043, 1989.

[7] Y. K. Lize, R. Gomma, R. Kashyap, L. Palmer and a. A. E. Willner, "Fast all-fiber polarization scrambling using re-entrant Lefèvre controller," *Optics Commun*, vol. 279, pp. 50-52, 2007.

[8] F. Heismann, "Compact electro-optic polarization scramblers for optically amplified lightwave systems," *J. Lightwave Technol.*, vol. 14, pp. 1801-1814, 1996.

[9] J.-W. Kim, S.-H. C. W.-S. Park and a. M.-C. Oh, "Integrated-optic polarization controllers incorporating polymer waveguide birefringence modulators," *Opt. Express,* vol. 20, pp. 12443-12448, 2012.

[10] "http://www.novoptel.de/Scrambling/EPS1000_flyer.pdf," [Online].

[11] http://www.newridgetech.com/nrt-2500.html.

[12] "http://www.generalphotonics.com/product/pcd-104-polarization-scrambler/".

[13] "http://www.keysight.com/en/pd-1365426-pn-N7785B/".

[14] S. M. C. Sergeyev, A. Rozhin and S. Turitsyn, "Vector solitons with locked and precessing states of polarization," *Opt.Expr.,* vol. 20, pp. 27434-27440, 2012.

[15] S. M. C. Sergeyev, E. Turitsyna, A. Rozhin, S. Turitsyn and K. Blow, "Spiral attractor created by vector solitons," *Light: Science and Applications,* vol. 3, 2014.

[16] M. Guasoni, P.-Y. Bony, S. Pitois, D. Sugny, A. Picozzi, H.-R. Jauslin and J. Fatome, "Fast Polarization Scrambler Based on Chaotic Dynamics in Optical Fibers," in *European Conference on Optical Communications ECOC 2014, paper Tu.1.4.5,* 2014.

[17] P. Bony, M. Guasoni, P. Morin, D. Sugny, A. Picozzi, H. Jauslin, S. Pitois and J. Fatome, "Temporal spying and concealing process in fibre-optic data transmission systems through polarization bypass," *Nat. Commun.,* vol. 5, p. 5:4678 doi: 10.1038/ncomms5678, 2014.

[18] J. Fatome, S. Pitois, P. Morin, E. Assemat, D. Sugny, A. Picozzi, H. Jauslin, G. Millot, V. Kozlov and S. Wabnitz, "A universal optical all fiber omnipolarizer," *Scientific Reports* , vol. 2, p. 938, 2012.

[19] P.-Y. Bony, M. Guasoni, E. Assémat, S. Pitois, D. Sugny, A. Picozzi, H. R. Jauslin and J. Fatome, "Optical flip-flop memory and data packet switching operation based on polarization bistability in a telecomunnication optical fiber," *J. Opt. Soc. Am. B,* vol. 30, pp. 2318-2325, 2013.

[20] A. Gaeta, R. Boyd, J. Ackerhalt and P. Milonni, "Instabilities and chaos in the polarizations of counterpropagating light fields," *Phys. Rev. Lett.,* vol. 58, pp. 2432-2435, 1987.

[21] D. J. Gauthier, M. S. Malcuit and a. R. Boyd, "Polarization Instabilities of Counterpropagating Laser Beams in Sodium Vapor," *Phys. Rev. Lett.,* vol. 61, pp. 1828-1830, 1987.

[22] E. Assémat, A. Picozzi, H. Jauslin and D. Sugny, "Hamiltonian tools for the analysis of optical polarization control," *J. Opt. Soc. Am. B* , vol. 29, pp. 559-571, 2012.

[23] M. Guasoni, E. Assémat, P. Morin, A. Picozzi, J. Fatome, S. Pitois, H. Jauslin, G. Millot and D. Sugny, "A line of polarization attraction in highly birefringent optical fibers," *J. Opt. Soc. Am. B,* vol. 31, pp. 572-580, 2014.

[24] V. Kozlov, J. Nuño and S. Wabnitz, "Theory of lossless polarization attraction in telecommunication fibers," *J. Opt. Soc. Am. B,* vol. 28, pp. 100-108, 2011.

[25] K. Turitsyn and S. Wabnitz, "Stability analysis of polarization attraction in optical fibers," *Opt. Commun.,* vol. 307, pp. 62-66, 2013.

[26] V. V. Kozlov, J. Fatome, P. Morin, S. Pitois, G. Millot and a. a. S. Wabnitz, "Nonlinear repolarization dynamics in optical fibers: transient polarization attraction," *J. Opt. Soc. Am. B,* vol. 28, pp. 1782-1791, 2011.

[27] P. Morin, J. Fatome, C. Finot, S. Pitois, R. Claveau and a. G. Millot, "All-optical nonlinear processing of both polarization state and intensity profile for 40 Gbit/s regenration applications," *Opt. Express,* vol. 19, pp. 17158-14166, 2011.

[28] A. Picozzi, J. Garnier, T. Hansson, P. Suret, S. Randoux, G. Millot and D. Christodoulides, "Optical wave turbulence," *Physics Reports,* vol. 1, p. 542, 2014.

[29] J. Goodman, Statistical Optics, Wiley Classics Library , 2000.

[30] J. H. V. Price et al, "Mid-IR supercontinuum generation from nonsilica microstructured optical fibers," *IEEE J. Sel. Top. Quantum Electron.,* vol. 13, pp. 738-750, 2007.

[31] C. Rosenberg Petersen, U. Moller, I. Kubat, B. Zhou, S. Dupont, J. Ramsay, T. Benson, S. Sujecki, N. Abdel-Moneim, Z. Tang, D. Furniss, A. Seddon and O. Bang, "Mid-infrared supercontinuum covering the 1.4-13.3 µm molecular fingerprint region using ultra-high NA chalcogenide step-index fibre," *Nat. Photon.,* DOI: 10.1038, 2014.

[32] O. Mouawad, J. Picot-Clémente, F. Amrani, C. Strutynski, J. Fatome, B. Kibler, F. Désévédavy, G. Gadret, J.-C. Jules, D. Deng, Y. Ohishi and F. Smektala, "Multioctave midinfrared supercontinuum generation in suspended-core chalcogenide fibers," *Opt. Let.,* vol. 39, pp. 2684-2687, 2014.

[33] L. Yao et al., "A novel scheme for achieving quasi-uniform rate polarization scramblingat 752 krad/s," *Optics Express,* vol. 20, p. 1691.

[34] C. Finot, B. Kibler, L. Provost and S. Wabnitz, "Beneficial impact of wave-breaking for coherent continuum formation in normally dispersive nonlinear fibers," *J. Opt. Soc. B,* vol. 25, pp. 1938-1948, 2008.

[35] D. J. Moss, R. Morandotti, A. L. Gaeta and a. M. Lipson, "New CMOS-compatible platforms based on silicon nitride and hydex for nonlinear optics," *Nature Photon. 7,* pp. 597-607, 2013.

[36] Razzari, L. Duchesne, D. Ferrera, M. Morandotti, R. Chu, S. Little and B. E. & Moss, "CMOS-compatible integrated optical hyper-parametric oscillator," *Nature Photon. 4,* pp. 41-45, 2010.

Massimiliano Guasoni was born in Verona, Italy, in 1982. He received the M.S. degree and the Ph.D. in Telecommunications from the University of Brescia (Italy) in 2007 and 2011, respectively, working on the subject of plasmonic waveguides. From 2010 to 2012 he was postdoctoral research fellow at the Department of Information Engineering of the University of Brescia (Italy), working on the subject of nonlinear cross-polarization interactions in photonic systems under the supervision of Pr. S.Wabnitz. Since 2013 he is postdoctoral research fellow at the Laboratoire Interdisciplinaire Carnot de Bourgogne of the University of Bourgogne, Dijon (France), working on the research project PETAL (*Polarization condEnsation for Telecom AppLications*), granted by the European Research Council and coordinated by Dr. J. Fatome. His main research interests are nonlinear optics, computational electromagnetism, plasmonics and photonics structures.

Pierre-Yves Bony was born in Langres, France, in 1989. After graduating with a scientific degree at Diderot high school of Langres and a DUT Mesures Physiques at the technological university institute (IUT) Léonard de Vinci of Reims, he got a Licence of Physics and then a Master Physique Laser & Matériaux (PLM) at the University of Burgundy of Dijon. In 2012, he began a Doctorate of Physics at the Interdisciplinary Carnot of Burgundy Laboratory (ICB) of Dijon. His subject deals with the all-optical control of the light polarization in telecommunication optical fibers and the new applications based on this concept. His thesis is an integrale part of the PETAL project directed by Julien Fatome.

Marin Gilles was born in Hyères, France in 1991. He received a Bachelor degree in Electronics, Energy and Automatism in 2011 and a Master degree in nanotechnology in 2013. He currently is a Ph.D. student at University of Bourgogne, France in the Solitons, Lasers and Optical Communications team. His research interest is in the study of light polarisation in optical fibers, how it can auto-organise within, the generation of solitonic structures and their propagation inside the fibers.

Antonio Picozzi was born in Monza, Italy, in 1971. He completed his studies at the University of Nice (France), including his PhD thesis in 1997 in the context of the resonant three-wave interaction modeling stimulated Brillouin or Raman effects. After a Post-Doc at ULB (Brussels) in which he studied the dynamics of quadratic nonlinear waves, he obtained in 2000 an associate Professor position at the University of Nice. At that time he started to work on nonlinear optics with partially coherent waves. Motivated by a close interaction with experimentalists, he obtained in 2005 a full research position at CNRS in the University of Burgundy (Dijon, France). In this way he was able to develop the theme of incoherent nonlinear optics through numerous collaborations as well as the supervision of PhD students and postdocs. This subject has reached a certain degree of maturation, especially with the development of a unified nonequilibrium thermodynamic formulation of statistical nonlinear optics (long-range wave turbulence in analogy with the Vlasov formulation of Gravitation, thermalization and condensation of nonlinear waves in analogy with the kinetic gas theory, spectral incoherent solitons in analogy with weak Langmuir turbulence in plasmas, or the breakdown of thermalization in analogy with the Fermi-Pasta-Ulam problem). He co-authored more than 80 articles in peer-reviewed journal, he has been invited to give more than 50 talks in international conferences and was promoted CNRS Research Director in 2013.

Julien Fatome was born in Charleville-Mézières, France, in 1978. After graduating from the engineer school ESIREM, he received the Master's degree in 2000 and the Ph.D. degree in physics for studies of ultra-short pulse propagation at 160-Gb/s in dispersion managed optical fiber lines in 2004, from the University of Bourgogne, Dijon, France. In 2005, he became a Research Engineer in the Centre National de la Recherche Scientifique (CNRS), Department of Physics, ICB, University of Bourgogne. He is currently carrying out research on nonlinear effects in optical fibers and ultrahigh bit rate optical communications, in particular on the all-optical control of light state of polarization. He has published over 160 contributions in peer-reviewed journals and conference proceedings and 4 patents. He is currently leading the ERC starting grant PETAL project.